processes

MDPI

Article

Pore Structure Change in the Continental Shale Oil Reservoir and Its Main Influencing Factors: A Case Study of the Chang 7 Member in the Ordos Basin

Xin He [1], Shijia Chen [1,2,3,*], Cong Hu [4], Haifeng Zhang [4], Feisheng Mou [1], Linfeng Dai [1], Yifan Lu [1], Xiaoyan Fu [1] and Meimei Han [1]

[1] School of Geoscience and Technology, Southwest Petroleum University, Chengdu 610500, China; 202111000042@stu.swpu.edu.cn (X.H.); 202121000145@stu.swpu.edu.cn (F.M.); 202121000068@stu.swpu.edu.cn (L.D.); 202121000065@stu.swpu.edu.cn (Y.L.); 202111000037@stu.swpu.edu.cn (X.F.); 202211000088@stu.swpu.edu.cn (M.H.)
[2] Natural Gas Geology Key Laboratory of Sichuan Province, Chengdu 610500, China
[3] State Key Laboratory of Oil and Gas Reservoir Geology and Exploitation, Chengdu 610500, China
[4] Changqing Oilfield Company, Xi'an 710018, China; hz520_cq@petrochina.com.cn (C.H.); zhfeng_cq@petrochina.com.cn (H.Z.)
* Correspondence: 199131010015@swpu.edu.cn; Tel.: +86-13880948696

Abstract: Shale oil in the Chang 7 member is the main target for further exploration in the Ordos Basin. However, the lack of research on the characteristics of the Chang 7 member's mudstone and shale reservoir has seriously affected the next stage of exploration for shale oil in the Chang 7 member. This study analyzed in detail the changes in the pore structure of different types of reservoirs and their influencing factors in detail through experiments such as gas adsorption, nuclear magnetic resonance, and high-pressure mercury intrusion. The results showed that black shale is mainly composed of micropores, with a micropore ratio of up to 79.88%. Dark mudstone and silty mudstone are mainly composed of mesopores, with a mesopore ratio greater than 30%. Argillaceous sandstone is mainly composed of large pores, accounting for 78.57%. From black shale to muddy sandstone, the proportion of micropores decreases, while the proportion of macropores increases. The micropore volume is mainly controlled by the organic matter content and the inorganic mineral content related to the organic matter content. Inorganic minerals such as quartz and feldspar mainly control the degree of development of mesopores and macropores. For rocks with a strong hydrocarbon-generating ability (black shale and dark mudstone), the ratio between the total pore volume and micropore volume is the main factor restricting their oil content. For rocks with a weak hydrocarbon-generating capacity (silty mudstone and argillaceous sandstone), the macropore volume and total pore volume are the main controlling factors for oil content. The results of this study have important guiding significance for the next step of exploration and development for shale oil in the Chang 7 member and, to a certain degree, for the exploration of continental shale oil in other basins.

Keywords: Ordos Basin; Chang 7 member; shale oil; reservoir; influencing factors; oil content

Citation: He, X.; Chen, S.; Hu, C.; Zhang, H.; Mou, F.; Dai, L.; Lu, Y.; Fu, X.; Han, M. Pore Structure Change in the Continental Shale Oil Reservoir and Its Main Influencing Factors: A Case Study of the Chang 7 Member in the Ordos Basin. *Processes* **2023**, *11*, 2314. https://doi.org/10.3390/pr11082314

Academic Editors: Yinhui Zuo and Hui Han

Received: 19 June 2023
Revised: 26 July 2023
Accepted: 30 July 2023
Published: 1 August 2023

1. Introduction

As the second largest country in terms of energy consumption, China's tension between oil and gas production and their demand is becoming increasingly severe, and its dependence on foreign countries for oil and gas is gradually increasing [1,2]. Meanwhile, as the recoverable reserves of conventional oil and gas resources are gradually decreasing, unconventional oil and gas reservoirs have become the main target and are important alternative resources for onshore crude oil exploration in China [3–5]. Compared with traditional oil and gas resources, shale oil has the advantages of having a wide distribution area, large resources, a long production cycle, etc. [6–10]. From a long-term perspective,

shale oil will be an important resource for long-term stable oil and gas production in the future, and it will provide the main support for China's crude oil [11–14].

The Ordos Basin is one of the hydrocarbon-bearing basins with abundant shale oil resources in China [15–18]. The maximum expansion period of the Ordos Basin was during the sedimentary period of the Chang 7 member. During this period, the lake was deep and wide, depositing a set of organic rich oil source rocks mainly composed of black shale and dark mudstone, with a thickness of over 100 m [19–22]. The Chang 7 member is not only the main source rock of the Yanchang formation but also the main interval for the development of shale oil. Compared with shale oil in other domestic basins, Chang 7 shale oil has high oil saturation, wide distribution, and broader exploration and development prospects. However, because most of the previous explorations that regarded the Chang 7 member as a source rock, the geochemical characteristics of the Chang 7 member source rock were mainly analyzed through geochemical and other experimental methods. Consequently, it was not regarded as a shale oil exploration layer, resulting in an incomplete shale reservoir evaluation of the formation [23–25]. The reservoir is the direct target layer of oil and gas exploration and research, and it is the main object of the oilfield's development. The fine characterization and comprehensive evaluation of shale oil reservoirs can provide a relatively reliable scientific basis for the exploration and development of shale oil, thereby improving the efficiency of exploration and development and increasing production efficiency. This is conducive to opening up a new branch of shale oil research in the Chang 7 member of the Ordos Basin and has important scientific value.

At present, research on shale reservoir's characteristics is mainly divided into two categories: ray detection technology and fluid injection technology. The ray type is a method and technology that utilizes optical, electronic, neutron, and other rays to characterize pores. Fluids mainly refer to fluids that do not undergo significant chemical reactions with the sample through injection. Based on the amount of fluid entering and the injection process, different theoretical methods have been used to quantitatively characterize pore structure parameters based on specific hypothetical models, including average pore size, pore volume, specific surface area, and pore size distribution [26–32]. We have drawn upon and applied the shale exploration and development technologies and achievements that have been made to carry out a fine characterization of the Chang 7 member shale oil reservoirs [33–35].

Based on this approach, this study used scanning electron microscopy, X-ray diffraction, high-pressure mercury intrusion, gas adsorption, and nuclear magnetic resonance (NMR) to analyze the rock mineralogy, pore structure, and oil-bearing characteristics of the Chang 7 member shale oil reservoir. The influencing factors of the reservoir's pore structure and its relationship with oil content are discussed. This study provides a theoretical basis for the next step of shale oil exploration and development in this area.

2. Geological Background

The Ordos Basin, China's second-largest sedimentary basin, covers an area of 370,000 km^2. The basin is bounded by Daqingshan Mountain in the north, Ziwuling Mountain in the south, Hailun Mountain and Mount Liupan in the west, and the Luliang Mountains in the east [36–38] (Figure 1). The study area was located in the southwest portion of the Ordos Basin, which belongs to the Yixia slope. It is a sedimentary lake basin with a low center and high periphery [39].

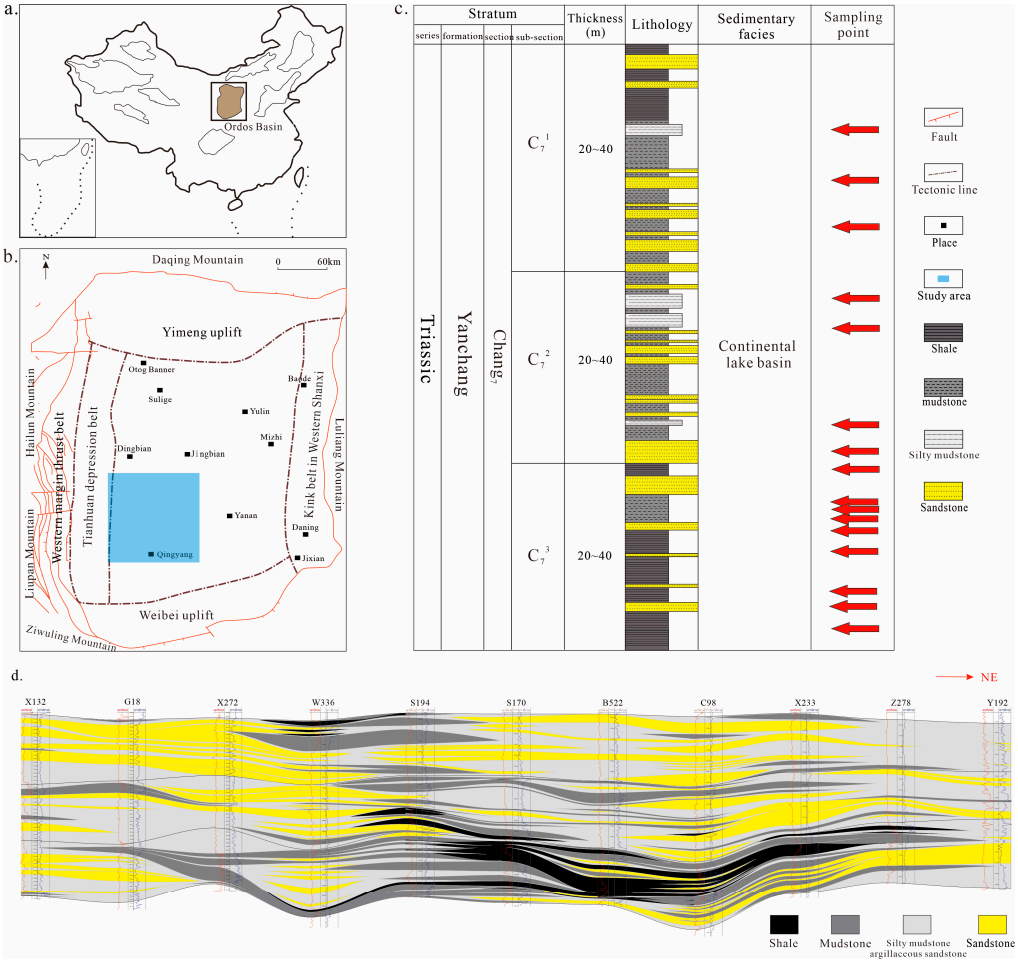

Figure 1. (**a**) Map of China; (**b**) Map of the Ordos Basin; (**c**) Comprehensive Histogram of Lithology in Chang 7 member; (**d**) Chang 7 member well profile.

Based on the actual demand of oil and gas exploration and production, the CNPC Changqing oilfield, in combination with the characteristics of logging curves, the cyclicity of sedimentary strata, and oil and gas bearing properties, divides the Upper Triassic Yanchang Formation into Chang 1 to Chang 10 oil-bearing formations from top to bottom. Among them, the interior of the Chang 7 oil layer group is divided into three sub layers from top to bottom, namely Chang 7_1, Chang 7_2, and Chang 7_3. During the depositional period of the Chang 7 member, the paleoclimate of the Ordos Basin was warm and humid, and a typical freshwater lake basin developed. Anoxic reduction in ancient water bodies is conducive to the preservation of sedimentary organic matter [40,41]. The sedimentary period of the Chang 7 member was the largest lake flooding period and the peak period of lake thermal fluid activity. The flourishing of algae and plankton laid the material foundation for the deposition of organic-rich shale during this period [42]. Therefore, the Chang 7 member is the main stratum for shale oil exploration in the Ordos Basin.

3. Materials and Methods

3.1. Materials

We collected 4 samples of each of the following: black shale, dark mudstone, silty mudstone, and argillaceous sandstone. These were collected from the Chang 7 member in different areas of the Ordos Basin, totaling 16 samples (Figure 2) (Table 1). We analyzed the mineral composition of different lithologies and selected 11 samples (3 black shale, dark mudstone, and silty mudstone and 2 argillaceous sandstone samples) to analyze the characteristics of different lithologic reservoirs in the Chang 7 member.

Figure 2. Photos of some samples.

Table 1. Description of samples.

Number	Well	Depth (m)	Horizon	Lithology Description
w-1	L254	2560.0	$C7_3$	Black shale
w-2	Z40	1460.4	$C7_3$	Black shale
w-3	B522	1957.6	$C7_3$	Black shale
w-4	Z233	1813.9	$C7_3$	Black shale
x-1	W336	2060.8	$C7_3$	Dark mudstone
x-2	H261	2244.5	$C7_3$	Dark mudstone
x-3	L211	2354.6	$C7_3$	Dark mudstone
x-4	L254	2581.5	$C7_3$	Dark mudstone
y-1	H317	2447.1	$C7_2$	Silty mudstone
y-2	X233	1984.9	$C7_2$	Silty mudstone
y-3	D214	1147.1	$C7_2$	Silty mudstone
y-4	Z233	1751.5	$C7_1$	Silty mudstone
z-1	W336	1976.0	$C7_1$	Argillaceous sandstone
z-2	H317	2452.2	$C7_2$	Argillaceous sandstone
z-3	N76	1713.1	$C7_1$	Argillaceous sandstone
z-4	Z233	1808.5	$C7_3$	Argillaceous sandstone

3.2. Methods

3.2.1. X-ray Diffraction

X-ray diffraction analysis is currently a simple and efficient experimental method to identify, analyze, and quantify the characteristics of shale mineral composition. A small sample of shale was first ground to 200 mesh and dried at 110 °C. The Panalytical X' Pert PRO X-ray diffractometer was used in the experiment. This instrument is manufactured by Panaco in the Netherlands. Equipped with a Co target, the instrument operates at 31 kV and 0.4 mA. Diffraction angles (2θ) were measured over a range of 3~55° with a scan interval of 0.02° (2θ). Semi-quantitative analysis was performed using X-Powder software. This software is the 2017 version of X-power software.

3.2.2. Scanning Electron Microscopy

The shale samples were prepared into rectangular blocks with a length of 8 mm, a width of 8 mm, and a height of 3 mm, and they were then ground with ultra-thin emery paper with particle sizes of 30 μm, 15 μm, 9 μm, 6 μm, 3 μm, 1 μm, and 0.1 μm until the surface was flat. Then, polishing was performed under vacuum using a Hitachi IM 4000 argon ion polisher. The Hitachi IM 4000 argon ion polishing machine is produced by a Japanese electronics company. The polished thick shale samples were imaged with secondary electrons using a Hitachi dual-beam scanning electron microscope to obtain high-resolution pore images. The Scanning electron microscope is manufactured by Philips in the Netherlands.

3.2.3. Low Pressure Isothermal CO_2 Adsorption and N_2 Adsorption

First, approximately 3 g of shale samples were weighed and crushed into 60–120 mesh sample tubes, and then they were degassed and dried at 110 °C in a vacuum of less than 10 mmHg for more than 10 h to remove moisture and volatile substances. Low pressure isotherm adsorption experiments were performed on a Quantachrome NOVA4200e specific surface area analyzer and porosimeter. This instrument is manufactured by Beiside

Company in Beijing. Using high-purity CO_2 gas as the adsorbate, the adsorption isotherm of CO_2 at the mixing temperature of ice and water was obtained. During the experiment, the relative pressure (p/p0) was set in the range of 0.00001~0.03. N_2 adsorption using high-purity N_2 as the adsorbate was performed; the adsorption isotherm curve was obtained at the temperature of liquid nitrogen, and the relative pressure was set in the range of 0.005–0.995 during the experiment.

3.2.4. High-Pressure Mercury Intrusion

The sample was cut into small squares of 1 cm^3 with a cutting machine, and the pore structure data of the sample was obtained via automatic mercury intrusion.

3.2.5. NMR

Plunger samples were used for the NMR experiments. The samples were placed in a closed saturated device and evacuated for 1 h to remove air and adsorbed impurities in the samples. Then, the samples were saturated with a 5% NaCl solution at a fluid pressure of 30 MPa for 24 h for NMR testing. In the fully saturated NMR test, the solution adhering to the surface of the sample needed to be wiped off with wet filter paper as these non-porous fluids can affect the accuracy of test results. The nuclear magnetic resonance experimental instrument was a MesoMR23/12-060H-I nuclear magnetic resonance instrument produced by the Suzhou Niu Mai Company (Suzhou, China). The magnetic field strength was 0.3 ± 0.03 T, and the main frequency (SF) was 12 MHz. NMR T_2 analysis adopted a CPMG echo sequence. The experimental parameters were set as follows: echo interval time (TE), 0.1 ms; echo number (NECH), 16,000; waiting time (TW), 6000 ms; and scan number (NS), 32.

3.2.6. Tools and Methods for Drawing Graphics

All graphics were drawn using Excel, CDR, and Origin software to ensure that the clarity and resolution of the images meet the requirements of the journal. All software is version 2021.

4. Result

4.1. Mineralogy and the Microscopic Characteristics of Different Types of Shale Oil Reservoirs

The whole-rock minerals and clay minerals were tested and analyzed with X-ray diffraction experiments, and the experimental results are shown in Figure 3. The main mineral components of shale oil reservoirs in the Chang 7 member of the Ordos Basin were brittle minerals, with a content of 53.3~88.2% and an average of 65.0%. Among the brittle minerals, the quartz content was the highest, ranging from 24.8% to 55.4%, with an average of 42.8%. The feldspar content ranged from 5.5% to 32.8%, with an average of 16.1%. Most samples contained more pyrite, up to 33.5%. This is followed by clay minerals; the content was 11.8~46.3%, with an average of 31.2%. The content of carbonate minerals was less, mainly made up of dolomite, at up to 14.5%. Clay minerals, carbonate minerals (quartz + feldspar + pyrite), and carbonate minerals (calcite + dolomite + siderite) were used as three endmembers to make a triangular diagram, with the content of each being 50% as the boundary (Figure 3a). This shows that the lithofacies of different lithologies were relatively concentrated, and all were dominated by siliceous mud shale.

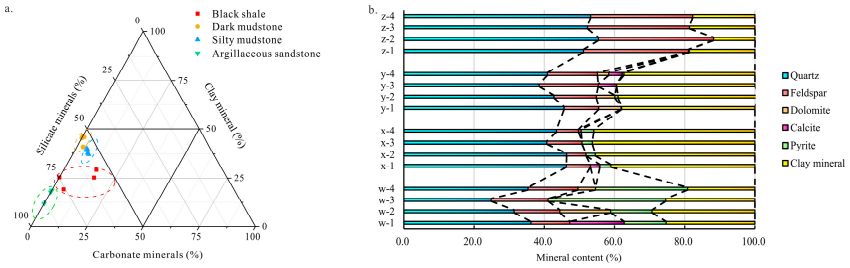

Figure 3. (**a**) Triangle diagram of mineral composition; (**b**) Mineral composition percentage chart.

The compositions of different lithologic minerals were quite different. As is shown in Figure 3b, black shale tended to have a higher pyrite content, averaging 20.9%, representing the main difference from other lithologies. The dark mudstone had a higher clay mineral content, averaging 44.7%, which was different from other lithologies. The mineral composition of silty mudstone is similar to that of dark mudstone, making it difficult to distinguish. The only difference is that the dark mudstone contains a small amount of pyrite, while the silty mudstone contains almost no pyrite. The content of quartz and feldspar in the argillaceous sandstone was higher, which was different from the other lithology.

At the same time, we used microscopy and scanning electron microscopy to better observe the differences between the different types of shale oil reservoirs.

The reflected light and fluorescence characteristics were observed with a polarized light microscope, and it was found that the black shale had an obvious bedding structure and strong fluorescence. Dark mudstone and silty mudstone had no bedding structure. The fluorescence of dark mudstone was strong, and the fluorescence of silty mudstone was almost invisible, indicating that the oil content of dark mudstone is much better than that of silty mudstone. In the argillaceous sandstone, quartz and feldspar particles could be seen under the microscope, and the fluorescence was strong, indicating that the rock has a high oil content (Figure 4).

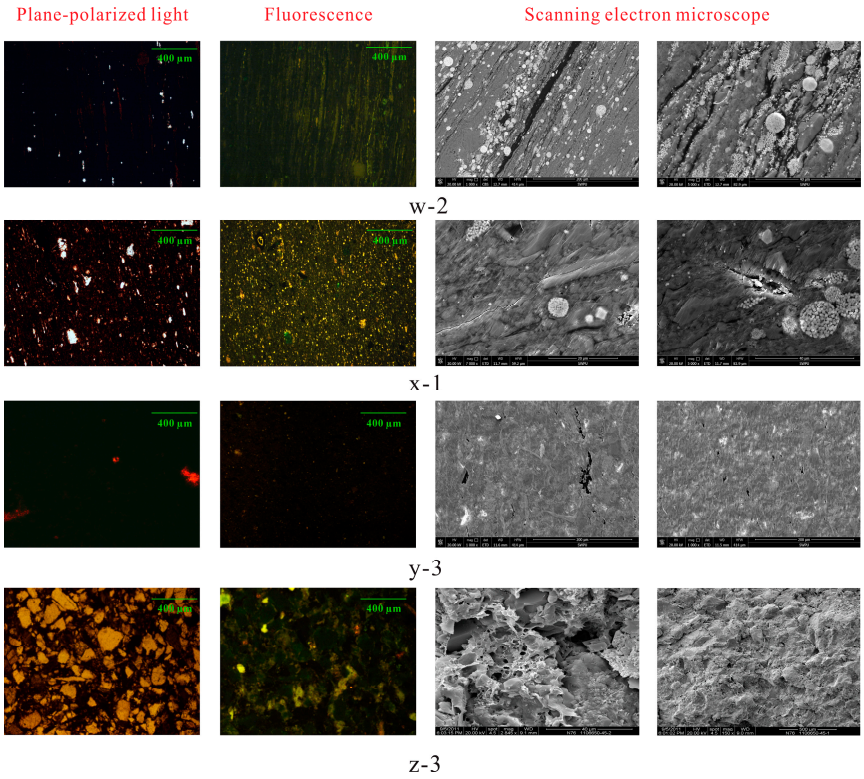

Figure 4. Microscopic characteristics of different types of shale oil reservoirs.

Scanning electron microscopy observation showed that the organic matter of black shale was distributed in strips, often coexisting with a large number of clusters of pyrite. There were basically no pores related to the organic matter in the shale, and the types of pores were mainly mineral matrix pores, bedding fractures, pyrite intracrystalline pores, and other fractures. The content of organic matter and pyrite in the dark mudstone was greatly reduced, the organic matter was distributed massively, and there were mineral matrix pores and cracks such as micro-cracks and interlayer pores of clay ore. The silty mudstone basically did not contain pyrite, and the organic matter was sporadically distributed in the form of agglomerates. The argillaceous sandstone basically did not contain organic matter, but the pores were relatively developed, mainly being intergranular pores and clastic particle dissolution pores (Figure 4).

4.2. Geochemical Characteristics

The organic matter abundance and oil content of different types of shale oil reservoirs were different. Among them, the TOC (total organic carbon) of black shale was the largest, at levels between 21.72% and 26.15%, with an average of 23.57%. The largest was dark mudstone, with an average of 5.66%. Both black shale and dark mudstone are good source rocks. The abundance of organic matter in silty mudstone and argillaceous sandstone was relatively poor, with an average of 1.30% and 0.83%, respectively. In terms of oil content, argillaceous sandstone had the highest oil content, with an average S_1 of 8.48 mg/g. Black shale and dark mudstone had slightly lower oil contents, with an average S_1 of 4.35 mg/g and 2.23 mg/g, respectively. The silty mudstone had the lowest oil content, with an average of 1.30 mg/g (Table 2).

Table 2. Partial experimental data of different samples.

Number	TOC (%)	S_1 (mg/g)	S_2 (mg/g)	Tmax (°C)	Max CO_2 Adsorption Capacity (mL/g)	Max N_2 Adsorption Capacity (mL/g)	Max Mercury Intake Volume (mL/g)	NMR Porosity (%)
w-1	26.15	5.35	41.98	453	8.51	3.07	0.00617	5.53
w-2	21.72	3.54	48.95	434	5.31	0.92	0.00586	3.13
w-3	22.86	4.16	38.62	447	3.36	1.97	0.00584	1.71
Mean value	23.57	4.35	43.18	445	5.73	1.99	0.00596	3.46
x-1	8.16	2.16	28.75	450	3.62	10.58	0.01183	4.06
x-2	3.03	1.92	6.63	448	3.01	8.63	0.00777	4.45
x-3	5.78	2.62	23.40	432	2.96	7.54	0.01201	3.46
Mean value	5.66	2.23	19.59	443	3.20	8.92	0.01054	3.99
y-1	1.03	0.91	0.13	465	2.29	7.64	0.01472	3.45
y-2	1.05	0.66	0.38	451	0.84	6.84	0.01032	2.73
y-3	1.82	0.62	0.26	461	2.48	6.57	0.02053	3.64
Mean value	1.30	0.73	0.26	459	1.87	7.02	0.01519	3.27
z-1	0.82	8.65	0.56	462	2.07	6.94	0.04745	9.10
z-2	0.84	8.30	0.72	468	0.77	5.05	0.05423	7.59
Mean value	0.83	8.48	0.64	465	1.42	6.00	0.05084	8.35

The maturity difference in different samples was minor, and the overall distribution was between 430 °C and 470 °C, which was in the mature stage.

4.3. Gas Adsorption

4.3.1. CO_2 Adsorption

The CO_2 adsorption curves of different samples are shown in Figure 5, and the curve shapes of the samples were similar. According to the latest classification of gas physical adsorption isotherms recommended by the IUPAC [43], the CO_2 adsorption curve of shale showed typical adsorption characteristics of type Ib solid microporous/mesoporous materials. Several types of shale oil reservoirs had obvious differences in the adsorption capacity of CO_2. The black shale had the largest adsorption capacity of CO_2, and the total adsorption capacity was between 3.36 mL/g and 8.51 mL/g, with an average of 5.73 mL/g. Second was the dark mudstone, and the total adsorption capacity was between 2.96 mL/g and 3.62 mL/g, with an average of 3.20 mL/g. The silty mudstone and argillaceous

sandstone had a poor CO_2 adsorption capacity, with an average adsorption capacity of 1.87 mL/g and 1.42 mL/g, respectively (Table 2).

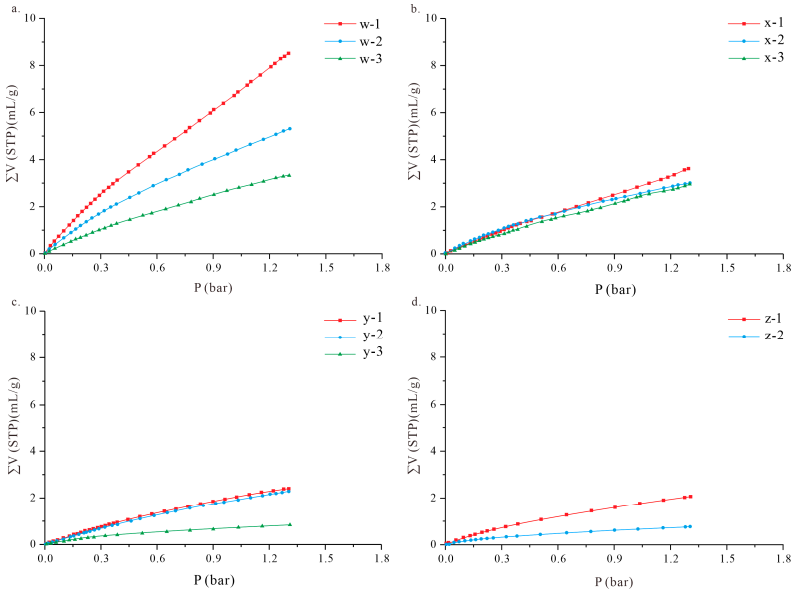

Figure 5. (**a**) CO_2 adsorption curve of black shale; (**b**) CO_2 adsorption curve of dark mudstone; (**c**) CO_2 adsorption curve of silty mudstone; (**d**) CO_2 adsorption curve of argillaceous sandstone.

4.3.2. N_2 Adsorption

The N_2 adsorption curves of different samples are shown in Figure 6. There was a difference in the shape of the curve for each sample. The N_2 adsorption curve of black shale showed typical adsorption properties of type IV H4 solid mesoporous materials. This indicates that the black shale was dominated by micropores and mesopores and contained some narrow fractures. The N_2 adsorption curves of other types of reservoirs showed predominantly typical adsorption characteristics of type IV H3 type solid mesoporous materials, and some samples were the H4 type. This was similar to the platelet-like granular material clay, reflecting the presence of a certain amount of clay mineral pores in the sample.

The dark mudstone had the largest adsorption capacity of N_2, and the total adsorption capacity was between 7.54 mL/g and 10.58 mL/g, with an average of 8.92 mL/g. The black shale had the smallest adsorption capacity, and the total adsorption capacity was between 0.92 mL/g and 3.07 mL/g, with an average of 1.99 mL/g. The N_2 adsorption capacity of silty mudstone and argillaceous sandstone were between those of dark mudstone and black shale, with an average adsorption capacity of 7.02 mL/g and 6.00 mL/g, respectively (Table 2).

4.4. High Pressure Mercury Intrusion

The mercury intrusion and mercury emission curves of different samples are shown in Figure 7. The mercury intrusion curves of the samples were basically similar. The mercury intrusion curves of different samples can be divided into three stages: the low-pressure rapid mercury injection stage (pressure was less than 1 psia), the medium-pressure boost stage (the pressure was between 1 psia and 3000 psia), and the high-pressure swift mercury injection stage (the pressure was greater than 3000 psia). Among them, black shale, dark mudstone, and silty mudstone had the largest mercury content in the high-pressure stage, indicating that the shale is dominated by smaller pores. The argillaceous sandstone contained a large amount of mercury in the low- and medium-pressure stages. This showed that it is mainly dominated by larger pores. The amount of total mercury injected was significantly different for each sample. The argillaceous sandstone had the largest amount of mercury injection, and the average mercury injection amount could reach 0.05084 mL/g.

In contrast, the black shale had the smallest amount of mercury injection, and the average total mercury injection amount was 0.00596 mL/g.

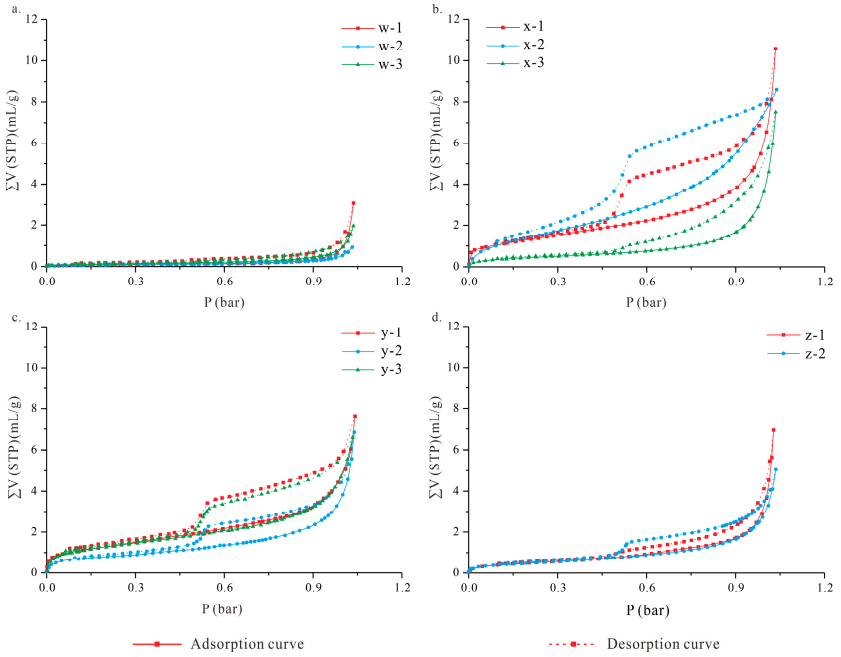

Figure 6. (**a**) N_2 adsorption curve of black shale; (**b**) N_2 adsorption curve of dark mudstone; (**c**) N_2 adsorption curve of silty mudstone; (**d**) N_2 adsorption curve of argillaceous sandstone.

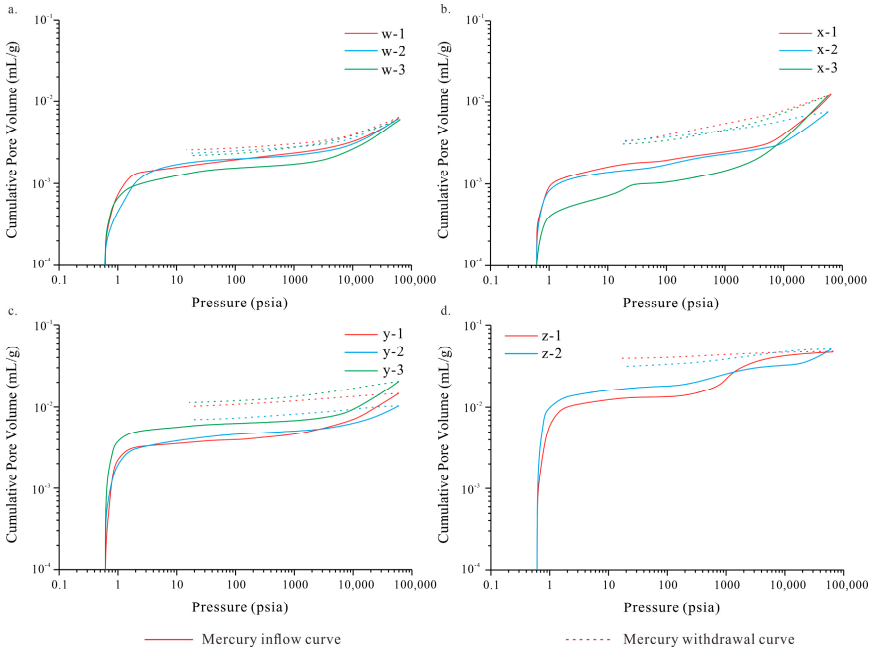

Figure 7. (**a**) Intrusive mercury curve of black shale; (**b**) Intrusive mercury curve of dark mudstone; (**c**) Intrusive Mercury curve of silty mudstone; (**d**) Intrusive mercury curve of argillaceous sandstone.

The mercury discharge curve was obviously different from the mercury injection curve. The mercury discharge curve of most samples was flat, and the mercury removal efficiency was low. Mercury injection and mercury removal cycle tests showed that a large amount of mercury remained in the pores of the samples. Mercury retention can reflect pore connectivity, and the greater the mercury retention, the worse the pore connectivity.

4.5. Nuclear Magnetic Resonance (NMR)

Through NMR analysis, it was observed that there were obvious differences in the NMR T_2 spectra of different samples (Figure 8).

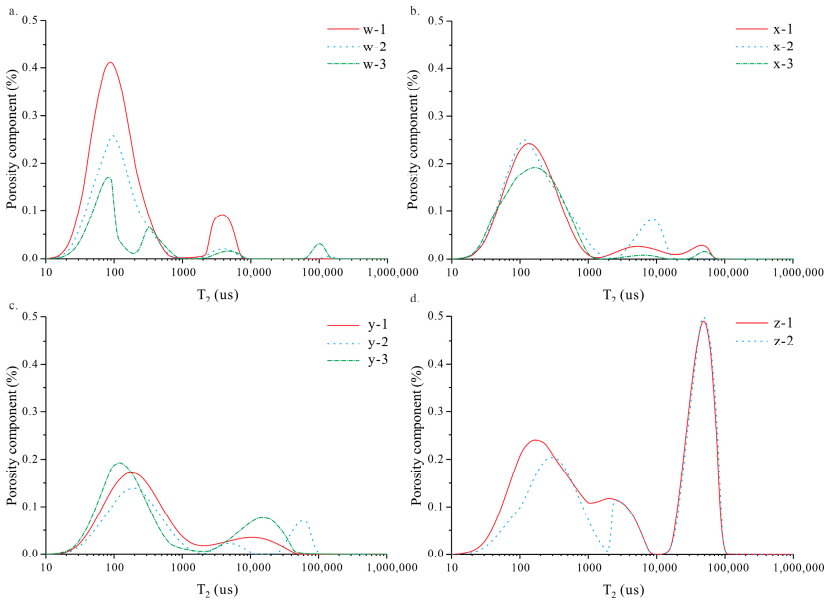

Figure 8. (**a**) NMR T_2 spectrum of black shale; (**b**) NMR T_2 spectrum of dark mudstone; (**c**) NMR T_2 spectrum of silty mudstone; (**d**) NMR T_2 spectrum of argillaceous sandstone.

The black shale T_2 time was mainly distributed within 100 ms, and the average NMR porosity was 3.46%, indicating that the reservoir is dominated by microscopic pores. The T_2 time of dark mudstone was mainly distributed within 1000 ms. Furthermore, the T_2 spectrum showed obvious three-peak characteristics, the average NMR porosity was 3.99%, and the storage performance was better than that of black shale. The T_2 time of silty mudstone was mainly distributed between 100 and 100,000 ms, and the average NMR porosity was 3.27%, indicating that the reservoir is highly heterogeneous. The T_2 time of argillaceous sandstone was mainly distributed in the range of more than 3000 ms, the average NMR porosity was 8.35%, and the reservoir physical properties were the best (Table 2).

5. Discussion

5.1. Characteristics of Reservoir Pore Structure

According to the pore classification method of the International Union of Theoretical and Applied Chemistry (IUPAC), pores are classified into micropores (<2 nm), mesopores (2~50 nm), and macropores (>50 nm). Since CO_2 molecules are able to enter pores with pore sizes as low as 0.35 nm, they can be used for micropore analysis. N_2 adsorption uses the capillary condensation principle to characterize the pore structure of shale. When capillary condensation occurs in macropores, the relative pressure is close to the saturated vapor pressure and cannot be measured accurately, so it is used to characterize mesopores [21,27]. The CO_2 adsorption mainly adopts the DFT theoretical calculation model (the theoretical calculation model has a small error, and the average error is 1%), and the N_2 adsorption mainly adopts the BJH theoretical calculation model. Mercury intrusion is used for macropore characterization because it is hard for mercury to enter small pores, which can cause shale pore deformation and ring failure. Of course, due to the intersection of the pore size measurement ranges of different experimental methods, only appropriate methods were used in the study to characterize the shale pore characteristics in different pore-size ranges. NMR itself can characterize the entire pore size of shale, and it can, therefore, be used for verification and as a reference for the above experimental methods.

5.1.1. Pore Size and Pore Volume Distribution Characteristics

The pore volume distribution curve of the samples in the study area is shown in Figure 9. The pore volume curves of all samples were multimodal. Black shale had a higher peak in the pore size range of 0.3~2 nm. Pores in this range contributed significantly to the total pore volume, averaging 79.88%. The contribution of mesopores to the pore volume of dark mudstone and silty mudstone was significantly greater than that of black shale, and the proportion was approximately 30%. The macropore volume of argillaceous sandstone was significantly larger than that of other lithologies, with an average proportion of 78.57%. From black shale to argillaceous sandstone, the proportion of micropores decreased, and the proportion of mesopores and macropores increased (Table 3).

The porosity of different lithologic samples was obtained according to the pore volume. Among them, the porosity of black shale was larger, ranging from 3.63% to 7.31%, with an average of 5.20%. The porosity of dark mudstone ranged from 4.49% to 5.94%, with an average of 5.31%. The silty mudstone had a low porosity, ranging from 3.40% to 5.03%, with an average of 4.41%. The argillaceous sandstone had the highest porosity, with an average of 9.21% (Table 3).

At the same time, we used nuclear magnetic resonance to analyze the pore volume distribution characteristics of different samples (Figure 10a). The experimental results were similar to those obtained in the above experiments. On the whole, in terms of black shale to argillaceous sandstone, it shows that the proportion of micropores was decreasing, and the proportion of mesopores and macropores was increasing. Of course, the porosity obtained by the two methods was different (Table 4), mainly in terms of micropores. The ratio of micropores obtained with NMR was significantly different from the experimental results obtained by combining various methods. For example, in black shale, the previous conclusion was that the micropore ratio was 79.88%, while the NMR results were approximately 50% (Table 4). We think that, mainly in the NMR tests, when the core pillars are saturated with water, it was difficult for water molecules to enter some tiny pores, causing the difference between the two. In particular, the larger the micropore volume, the larger the porosity difference between the two (Figure 10b). This also shows that there is a certain error in the characterization of pores smaller than 2 nm with NMR.

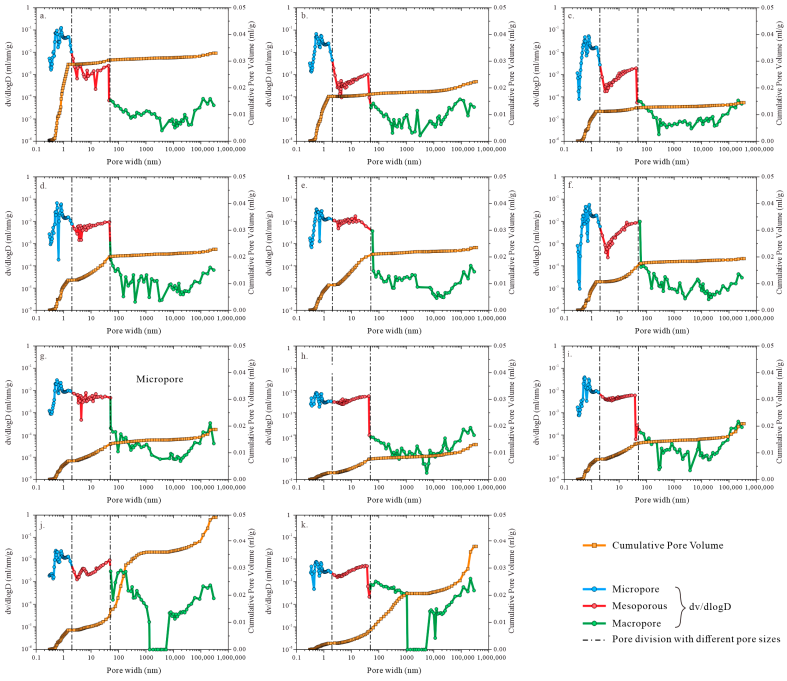

Figure 9. (**a**–**c**) Pore volume distribution curves of black shale; (**d**–**f**) Pore volume distribution curves of dark mudstone; (**g**–**i**) Pore volume distribution curves of silty mudstone; (**j**,**k**) Pore volume distribution curves of argillaceous sandstone.

Table 3. Multiple methods used together to characterize pore volume and pore specific surface area.

Number	Method	Pore Volume (mL/g)				Porosity (%)	Specific Surface Area (m^2/g)		
		Micropore	Mesoporous	Macropore	Total Pore		Micropore	Mesoporous	Macropore
w-1	Multi method combination	0.0288	0.0016	0.0026	0.0330	7.31	75.90	0.4399	0.0168
w-2		0.0168	0.0008	0.0048	0.0224	4.66	46.60	0.2243	0.0112
w-3		0.0112	0.0013	0.0020	0.0145	3.63	30.30	0.3482	0.0143
x-1		0.0113	0.0087	0.0029	0.0229	5.52	30.60	0.0467	2.9033
x-2		0.0095	0.0105	0.0035	0.0235	5.94	27.00	4.9700	0.0941
x-3		0.0107	0.0051	0.0035	0.0194	4.49	27.80	1.3000	0.1408
y-1		0.0069	0.0052	0.0066	0.0187	4.80	19.50	2.3400	0.1228
y-2		0.0025	0.0051	0.0055	0.0131	3.40	7.66	1.8257	0.0226
y-3		0.0075	0.0060	0.0074	0.0209	5.03	21.20	2.3713	0.0356
z-1		0.0072	0.0052	0.0367	0.0491	10.04	19.50	1.5700	1.0446
z-2		0.0023	0.0044	0.0313	0.0380	8.38	6.88	1.4034	0.1696

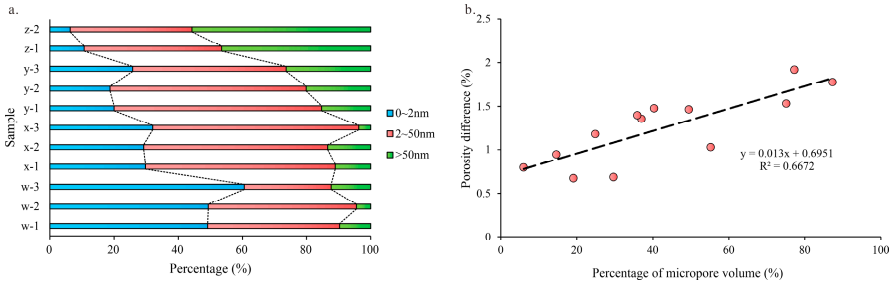

Figure 10. (**a**) The porosity ratio of different pore sizes using NMR; (**b**) the difference in porosity obtained with the two methods.

Table 4. NMR characterization of pore volume.

Number	Method	Porosity Component (%)			Percentage (%)			NMR Porosity (%)	Difference Value of Porosity (%)
		Micropore	Mesoporous	Macropore	Micropore	Mesoporous	Macropore		
w-1	NMR	2.72	2.27	0.54	49.19	41.05	9.76	5.53	1.78
w-2		1.55	1.45	0.14	49.52	46.33	4.47	3.13	1.53
w-3		1.03	0.46	0.21	60.23	26.90	12.28	1.71	1.92
x-1		1.21	2.40	0.45	29.80	59.11	11.08	4.06	1.46
x-2		1.30	2.55	0.60	29.15	57.17	13.45	4.46	1.48
x-3		1.11	2.22	0.13	32.08	64.16	3.76	3.46	1.03
y-1		0.69	2.23	0.53	20.00	64.64	15.36	3.45	1.35
y-2		0.51	1.67	0.55	18.68	61.17	20.15	2.73	0.67
y-3		0.94	1.74	0.96	25.82	47.80	26.37	3.64	1.39
z-1		0.97	3.90	4.23	10.66	42.86	46.48	9.10	0.94
z-2		0.48	2.88	4.23	6.32	37.94	55.73	7.59	0.79

5.1.2. Distribution Characteristics of Specific Surface Area

The distribution characteristics of the specific surface area of the samples in the study area are shown in Figure 11. Micropores were the main contributor to the specific surface area of the samples, accounting for 90.63% of the total specific surface area on average. The contribution of mesopores and macropores to the surface area was relatively small, accounting for 7.81% and 1.56%, respectively.

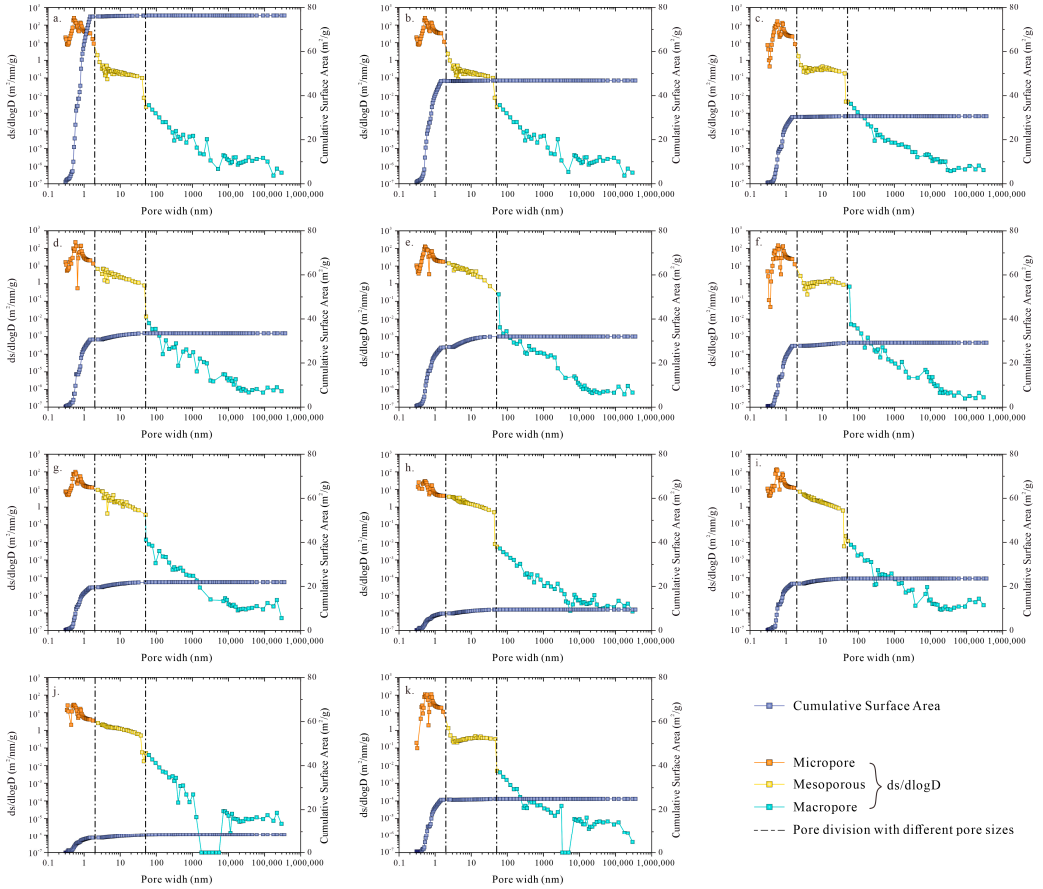

Figure 11. (**a**–**c**) Specific surface area distribution curves of black shale; (**d**–**f**) Specific surface area distribution curves of dark mudstone; (**g**–**i**) Specific surface area distribution curves of silty mudstone; (**j**,**k**) Specific surface area distribution curves of argillaceous sandstone.

Therefore, black shale and dark mudstone with the largest micropore volume, had the largest specific surface area, while silty mudstone and argillaceous sandstone had relatively small specific surface areas. Among them, the maximum specific surface area of black shale and silty mudstone could reach 76.36 m^2/g, with an average of 41.45 m^2/g. The maximum specific surface area of silty mudstone and argillaceous sandstone was 23.61 m^2/g, and the average was 17.13 m^2/g.

Samples with larger specific surface areas tend to have a stronger adsorption capacity. Therefore, the specific surface area distribution characteristics of different samples reflect, to a certain extent, that black shale and dark mudstone have a large number of tiny pores, and the crude oil in the pores is mostly in an adsorbed state. The silty mudstone and argillaceous sandstone have larger pores, and the crude oil in the pores is mostly in a free state.

5.2. Influencing Factors of Pore Structure

5.2.1. Effects of Different Mineral Contents on Pore Structure

For different lithologies in the study area, the effects of quartz, feldspar, pyrite, and clay minerals on the pore structure are shown in Figures 12 and 13. Overall, pore volume correlated well with the content of quartz, feldspar, and clay minerals, and it had the worst correlation with pyrite content.

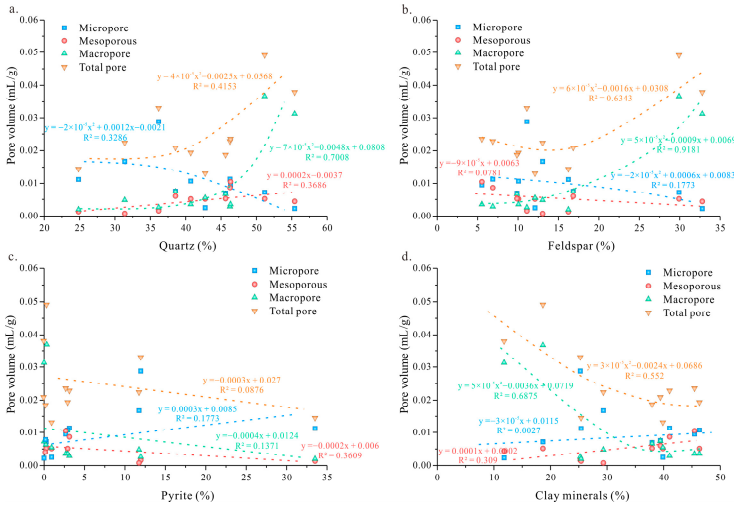

Figure 12. (**a**) Cross plot of quartz content and pore volume; (**b**) Cross plot of feldspar content and pore volume; (**c**) Cross plot of pyrite content and pore volume; (**d**) Cross plot of clay minerals content and pore volume.

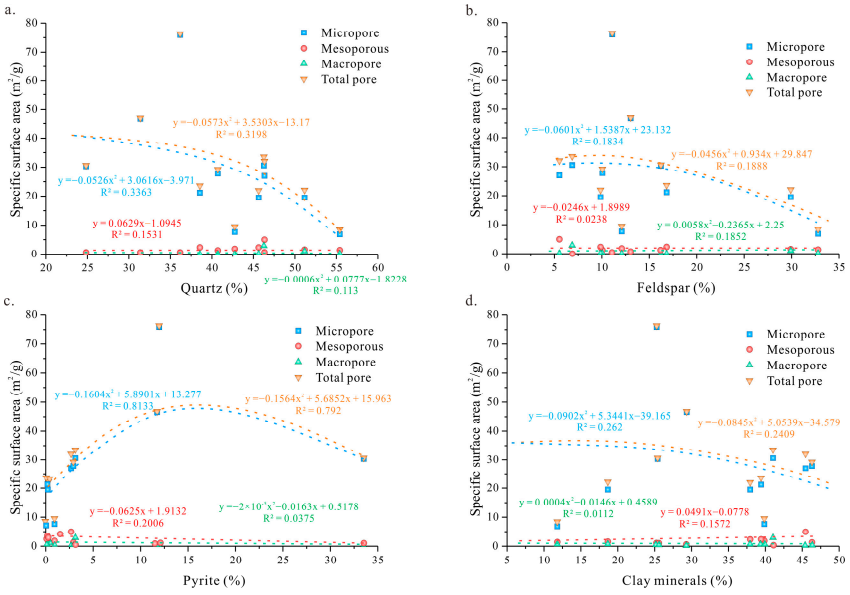

Figure 13. (**a**) Cross plot of quartz content and Specific Surface Area; (**b**) Cross plot of feldspar content and Specific Surface Area; (**c**) Cross plot of pyrite content and Specific Surface Area; (**d**) Cross plot of clay minerals content and Specific Surface Area.

Mesopore volume and micropore volume correlated poorly with different mineral contents. Among them, the correlation with quartz and pyrite was good, but the average correlation coefficient R^2 was only 0.3648 and 0.2530. Overall, mesopore volume was positively correlated with quartz and clay minerals and negatively correlated with feldspar and pyrite. Micropore volume was positively correlated with pyrite and clay minerals and negatively correlated with quartz and feldspar.

The macropore volume and total pore volume had the best correlations with quartz, feldspar, and clay minerals, with the average correlation coefficients R^2 of 0.7688 and 0.5339, respectively. The volume of macropores and total pores increased with the increase in quartz content. As the content of clay minerals increased, the macropore volume and total pore volume decreased. The total pore volume showed a trend of first decreasing and then increasing with the increase in feldspar content (Figure 12b). Further analysis revealed that this was due to the fact that, when the content of feldspar was low, there were

fewer macropores and more micropores and mesopores. The volume of micropores and mesopores was negatively correlated with the content of feldspar, resulting in a decrease in total pore volume with an increase in feldspar content. When the content of feldspar increased to a certain level, the number of macropores increased, while the number of micropores and mesopores decreased. The macropore volume was positively correlated with the content of feldspar, so the total pore volume increased with the increase in feldspar content.

In general, inorganic minerals have a large effect on macropore volume and the total pore volume, while the effect on micropore volume and mesopore volume is relatively small.

The correlation between the pore specific surface area of the samples and the content of inorganic minerals was generally poor, and the correlation coefficient R^2 was mostly less than 0.5 (Figure 13). However, the micropore specific surface area had a good correlation with the pyrite content, and the correlation coefficient R^2 could reach 0.8133. With the increase in pyrite content, the specific surface area of micropores first increased and then decreased. This is because an increase in pyrite content often represents an increase in organic matter content in rock samples, which promotes the development of micropores to a certain extent. However, when the pyrite content is too high, it is not conducive to the existence of organic matter to a certain extent, resulting in the poor development of micropores.

5.2.2. The Effect of TOC on Pore Structure

We analyzed the pore structure parameters of different samples in the study area under the condition of different TOC. The results showed that the micropore volume has the best correlation with TOC, and the correlation coefficient R^2 was 0.6984 (Figure 14a). With the increase in TOC, the micropore volume also increased, indicating that the organic matter content played a positive role in the development of micropores. However, with the increase in pore size, the correlation between TOC and pore volume gradually deteriorated, and the correlation coefficient R^2 between total pore volume and TOC was only 0.1698. This shows that TOC only controls the development of micropores in the rock pore system in the study area and has a weak influence on the development of the overall pores. This also shows that the development of pores related to organic matter in the study area was relatively poor.

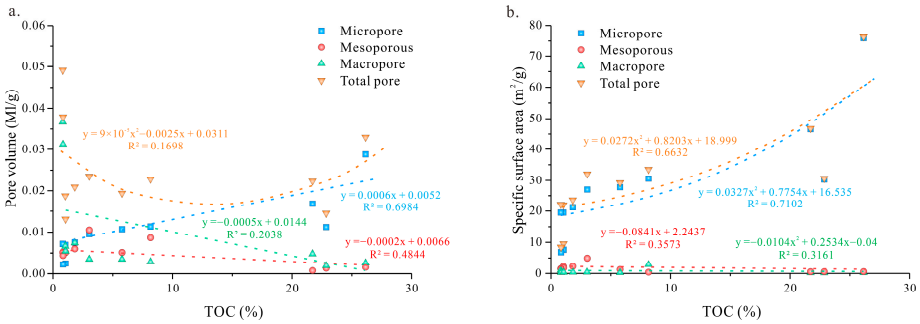

Figure 14. (**a**) Intersection diagram of pore volume and TOC; (**b**) Intersection diagram of TOC and specific surface area.

The correlation between TOC and specific surface area was better than that between TOC and pore volume. Among them, the correlation between the specific surface area of micropores and TOC was the best, and the correlation coefficient R^2 was 0.7102 (Figure 14b). The correlation between the specific surface area of macropores and mesopores is poor, and the correlation coefficient R^2 was 0.3573 and 0.3161, respectively. This shows that the contribution of organic matter to micropores was the largest, while the contribution to mesopores and macropores was relatively small. This is basically consistent with our previous understanding that organic matter mainly develops micropores.

In general, inorganic mineral content and organic matter content jointly control the development of the rock pore structure. The content of organic matter and the content of inorganic minerals related to organic matter mainly control the development of micropores. Inorganic minerals such as quartz and feldspar mainly control the development of mesopores and macropores.

5.3. Relationship between the Reservoir Pore Structure and Oil Content

As is shown in Figure 15, the oil content of the reservoir was mainly controlled by the pore volume, but it had a poor correlation with the specific surface area. Among them, macropore volume and total pore volume had the best correlation with the oil content of the rock, and the correlation coefficient R^2 was 0.6257 and 0.7441 respectively. The correlation between microporous volume and mesoporous volume and oil content was poor, and the correlation coefficient R^2 was 0.0081 and 0.1126, respectively. This indicates that the macropore volume has a great influence on the oil content of the reservoir. Therefore, the argillaceous sandstone with the largest proportion of macropore volume had the best oil content in all samples. Of course, macropore volume is not an absolute control factor of oil content. For black shale, the macropore volume was relatively poor, but the oil content was relatively good compared with dark mudstone and silty mudstone. This is mainly because the organic matter abundance of black shale is much higher than that of other lithology. At the same time, micropores are developed, and crude oil does not easily migrate. The generated crude oil can fill the whole pore space, resulting in a high oil content.

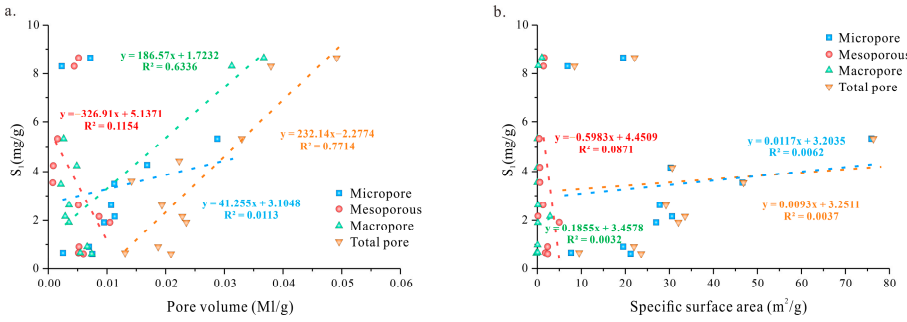

Figure 15. (**a**) Intersection diagram of pore volume and S_1; (**b**) Intersection diagram of specific surface area and S_1.

In conclusion, the influence of pore structure on oil content is mainly reflected in two aspects: preservation and migration. For the rocks with a strong hydrocarbon-generating capacity, the total pore volume and microporous volume are the main factors restricting the oil content. If the total pore volume is large and the crude oil storage space is large, the oil content of the reservoir is high. When the microporous volume is large, it is more difficult for crude oil to migrate out, and more is stored in the rock. Macropore volume and total pore volume are the main control factors for rocks with a weak hydrocarbon-generation capacity. Due to its weak hydrocarbon-generation capacity, most crude oil comes from an external supply. Therefore, the higher the degree of macropore development, the easier the crude oil is transported to the reservoir space, and the higher the oil content of the rock.

For the Chang 7 member of the Ordos Basin, mudstone and shale have a strong hydrocarbon-generating capacity, so the shale oil exploitation only needs to consider the size of the reservoir space. Therefore, argillaceous sandstone mixed with shale is the best exploration target for shale oil exploitation in the Ordos Basin.

6. Conclusions

In conclusion, based on various experimental methods, this paper has discussed the pore structure characteristics and influencing factors of different types of shale oil reservoirs in the Chang 7 member of the Ordos Basin and their relationship with oil-bearing characteristics. In the future, we will select more samples for relevant experiments in order

to further demonstrate the characteristics of the shale oil reservoir in the Chang 7 member. At the same time, we will conduct relevant research on the hydrocarbon generation and the expulsion mechanism of shale to clarify the hydrocarbon generation and expulsion characteristics of continental shale. The main conclusions of this paper are as follows.

(1) The shale oil reservoirs of the Chang 7 member in the Ordos Basin mainly include four types: black shale, dark mudstone, silty mudstone, and argillaceous sandstone. Among them, the black shale pyrite content was found to be high, and the average content of pyrite was 20.9%. Black shale exhibits an obvious bedding structure under both microscopy and scanning electron microscopy. The pyrite content of dark mudstone was found to be low. However, the content of clay minerals was higher than that of other lithology, and the average content of clay minerals was 44.7%. Under a scanning electron microscope, it could clearly be observed that the organic matter was distributed in blocks and strips, but there was no layered structure as a whole. The silty mudstone did not contain pyrite and had a low organic matter content, and the other mineral components were similar to those of dark mudstone. The content of quartz and feldspar in argillaceous sandstone was higher, which was different from other lithology.

(2) We combined various methods to characterize the pore structure of the reservoir. The results showed that the black shale was mainly composed of micropores, with an average volume of 0.0189 mL/g and a micropore ratio of 87.27% of the total volume. Dark mudstone and silty mudstone were mainly mesoporous, with an average mesoporous volume of 0.0068 mL/g and a proportion greater than 30%. Muddy sandstone was mainly composed of macropores, with a proportion of 78.57%. From black shale to muddy sandstone, the proportion of micropores decreased, while the proportion of mesopores and macropores is increased.

(3) Inorganic minerals and organic matter jointly control the development of the rock's pore structure. Among them, organic matter and inorganic minerals related to organic matter mainly control the development of micropores. Inorganic minerals such as quartz and feldspar mainly control the development of mesopores and macropores. The total pore volume has the best correlation with the content of quartz, feldspar, and clay minerals, and the correlation coefficients observed in the this study were 0.4153, 0.6343, and 0.552, respectively.

(4) For rocks with a strong hydrocarbon-generating capacity, the total pore volume and micropore volume are the main controlling factors for reservoir oil content. The total pore volume is large and can store more crude oil. The micropore volume is small, the crude oil is difficult to transport out, and the crude oil is easier to store. For rocks with a weak hydrocarbon-generating ability, crude oil mainly comes from exogenous sources, and macropore volume and total pore volume are the main controlling factors. The proportion of large pore volume is high, and it is easier for crude oil to migrate to the storage space.

Author Contributions: Writing—review and editing, formal analysis, writing—original draft preparation, X.H.; writing—review and editing, funding acquisition, data curation, S.C.; supervision, data curation, resources, C.H.; validation, supervision, H.Z.; software, F.M.; formal analysis, L.D.; investigation, Y.L.; formal analysis, X.F.; methodology, M.H. All authors have read and agreed to the published version of the manuscript.

Funding: This study was funded by the National Natural Science Foundation of China (Nos. 42072185 and 41872165), Science and Technology Cooperation Project of the CNPC-SWPU Innovation Alliance (Nos. 2020CX030000 and 2020CX050000).

Data Availability Statement: All data, models, and codes generated or used in the study appear in the submitted article.

Conflicts of Interest: The authors declare no conflict of interest.

References

1. Zhao, W.Z.; Hu, S.Y.; Hou, L.H. Connotation and strategic role of in-situ conversion processing of shale oil underground in the onshore China. *Pet. Explor. Dev.* **2018**, *45*, 3–12. [CrossRef]
2. Jia, C.Z. Challenges faced by the upstream development of China's petroleum industry and the direction of scientific and technological research in the future. *Acta Pet. Sin.* **2020**, *41*, 1445–1464.
3. Liu, Q.Y.; Wu, X.Q.; Wang, X.F.; Jin, Z.J.; Zhu, D.Y.; Meng, Q.Q.; Huang, S.P.; Liu, J.Y.; Fu, Q. Carbon and hydrogen isotopes of methane, ethane, and propane: A review of genetic identification of natural gas. *Earth Sci. Rev.* **2019**, *190*, 247–272. [CrossRef]
4. Ju, Y.W.; Wang, G.Z.; Li, S.Z.; Ying, S.; Suo, Y.H.; Somerville, L.; Li, W.Y.; He, B.Z.; Zheng, M.L.; Yu, K. Geodynamic mechanism and classification of basins in the earth system. *Gondwana Res.* **2020**, *102*, 200–228. [CrossRef]
5. Hu, T.; Pang, X.Q.; Jiang, F.J.; Wang, Q.F.; Wu, G.Y.; Liu, X.H.; Jiang, S.; Li, C.R.; Xu, T.W.; Chen, Y.Y. Key factors controlling shale oil enrichment in saline lacustrine rift basin: Implications from two shale oil wells in Dongpu Depression, Bohai Bay Basin. *Pet. Sci.* **2021**, *18*, 687–711. [CrossRef]
6. Aguilera, R.F.; Eggert, R.G.; Gustavo, L.; Tilton, J.E. Depletion and the future availability of petroleum resources. *Energy J.* **2009**, *30*, 141–174. [CrossRef]
7. Qian, X.M. Geological structure and oil and gas exploration of the eastern mediterranean. *J. Coast. Res.* **2020**, *36*, 119–123. [CrossRef]
8. Reynolds, D.B. World oil production trend: Comparing hubbert multi-cycle curves. *Ecol. Econ.* **2014**, *98*, 62–71. [CrossRef]
9. Bai, Y.H.; Hua, T.; Yan, K. Geological characteristics and some problems in development for oil shale in northwest China. *Oil Shale* **2011**, *28*, 380–397.
10. Chen, G.H.; Lu, S.F.; Zhang, J.F.; Wang, M.; Li, J.B.; Xu, C.X.; Pervukhina, M.; Wang, J. Estimation of enriched shale oil resource potential in e2s4l of Damintun sag in Bohai bay basin, China. *Energy Fuels* **2017**, *31*, 3635–3642. [CrossRef]
11. Basile, P.S.; Papin, A. World oil: A long-term look. *Energy* **1981**, *6*, 529–541. [CrossRef]
12. Harvie, B.A. Historical review paper the shale-oil industry in scotland 1858-1962. ii: Oil-shale quality, resources and technological advances. *Oil Shale* **2011**, *28*, 78–84. [CrossRef]
13. Hou, M.F.; Pan, S.Q.; Liu, H.L. The general trend of world energy transformation and China's oil and gas sustainable development strategy. *Nat. Gas Ind.* **2021**, *41*, 8.
14. Zou, C.N.; Zhu, R.K.; Wu, S.T.; Yang, Z.; Tao, S.Z.; Yuan, X.J.; Hou, L.H.; Hua, Y.; Xu, C.C.; Li, D.H.; et al. Types, characteristics, genesis and prospects of conventional and unconventional hydrocarbon accumulations: Taking tight oil and tight gas in China as an instance. *Shiyou Xuebao/Acta Pet. Sin.* **2012**, *33*, 173–187.
15. Li, D.L.; Li, R.X.; Zhu, Z.W.; Wu, X.L.; Cheng, J.H.; Liu, F.T.; Zhao, B.S. Origin of organic matter and paleo-sedimentary environment reconstruction of the Triassic oil shale in Tongchuan city, southern ordos basin (China). *Fuel* **2017**, *208*, 223–235. [CrossRef]
16. Lei, Y.H.; Luo, X.R.; Wang, X.Z.; Zhang, L.X.; Jiang, C.F.; Yang, W.; Yu, Y.X.; Cheng, M.; Zhang, L.K. Characteristics of silty laminae in Zhangjiatan shale of southeastern ordos basin, China: Implications for shale gas formation. *AAPG Bull.* **2015**, *99*, 661–687. [CrossRef]
17. Zhang, H.; Meng, X.Z. Distribution characteristics of the Triassic Yanchang formation Chang7 member oil shale and resource potential of shale gas, ordos basin. *Ground Water* **2013**, *2*, 93–96.
18. Tang, X.; Zhang, J.C.; Wang, X.Z.; Yu, B.S.; Ding, W.L.; Xiong, J.Y.; Yang, Y.T.; Wang, L.; Yang, C. Shale characteristics in the southeastern Ordos basin, China: Implications for hydrocarbon accumulation conditions and the potential of continental shales. *Int. J. Coal Geol.* **2014**, *128–129*, 32–46. [CrossRef]
19. Du, J.M.; Zhao, Y.D.; Wang, Q.C.; Yu, Y.Q.; Xiao, H.; Xie, X.K.; Du, Y.G.; Su, Z.M. Geochemical characteristics and resource potential analysis of Chang 7 organic-rich black shale in the Ordos basin. *Geol. Mag.* **2018**, *156*, 1–10. [CrossRef]
20. Bai, Y.L.; Ma, Y.H. Geology of the chang7 member oil shale of the yanchang formation of the Ordos basin in central north China. *Pet. Geosci.* **2019**, *26*, 355–371.
21. Li, T.W.; Jiang, Z.X.; Li, Z.; Wang, P.F.; Xu, C.L.; Liu, G.H.; Su, S.Y.; Ning, C.X. Continental shale pore structure characteristics and their controlling factors: A case study from the lower third member of the Shahejie formation, Zhanhua sag, eastern China. *J. Nat. Gas Sci. Eng.* **2017**, *45*, 670–692. [CrossRef]
22. Sun, L.N.; Tuo, J.C.; Zhang, M.F.; Wu, C.J.; Wang, Z.X.; Zheng, Y.W. Formation and development of the pore structure in chang7 member oil-shale from ordos basin during organic matter evolution induced by hydrous pyrolysis. *Fuel* **2015**, *158*, 549–557. [CrossRef]
23. Xu, Z.J.; Liu, L.F.; Wang, T.G.; Wu, K.J.; Dou, W.C.; Song, X.P. Analysis of the charging process of the lacustrine tight oil reservoir in the Triassic Chang 6 member in the southwest Ordos basin, China. *Can. J. Earth Sci.* **2017**, *54*, 1228–1247. [CrossRef]
24. Zou, C.N.; Guo, Q.L.; Yang, Z.; Wu, S.T.; Chen, N.S.; Lin, S.H.; Pan, S.Q. Resource potential and core area prediction of lacustrine tight oil: The Triassic Yanchang formation in Ordos basin, China. *AAPG Bull.* **2019**, *103*, 1493–1523. [CrossRef]
25. Jia, B.; Xian, C.G.; Tsau, J.S.; Zuo, X.; Jia, W.F. Status and Outlook of Oil Field Chemistry-Assisted Analysis during the Energy Transition Period. *Energy Fuels* **2022**, *36*, 12917–12945. [CrossRef]
26. Jia, B.; Xian, C.G. Permeability measurement of the fracture-matrix system with 3D embedded discrete fracture model. *Pet. Sci.* **2022**, *19*, 1757–1765. [CrossRef]

27. Chalmers, G.R.; Bustin, R.M.; Power, I.M. Characterization of gas shale pore systems by porosimetry, pycnometry, surface area, and field emission scanning electron microscopy/transmission electron microscopy image analyses: Examples from the Barnett, Woodford, Haynesville, Marcellus, and Doig units. *AAPG Bull.* **2012**, *96*, 1099–1119.
28. Clarkson, C.R.; Solano, N.R.; Bustin, R.M.; Bustin, A.M.M.; Blach, T.P. Pore structure characterization of North American shale gas reservoirs using USANS/SANS, gas adsorption, and mercury intrusion. *Fuel* **2013**, *103*, 606–616. [CrossRef]
29. Sun, M.D.; Yu, B.S.; Hu, Q.H.; Yang, R.; Zhang, Y.F.; Li, B. Pore connectivity and tracer migration of typical shales in south China. *Fuel* **2017**, *203*, 32–46. [CrossRef]
30. Anovitz, L.M.; Cole, D.R. Characterization and Analysis of Porosity and Pore Structures. *Rev. Mineral. Geochem.* **2015**, *80*, 61–164. [CrossRef]
31. Abdelsalam, S.I.; Alsharif, A.M.; Elmaboud, Y.A.; Abdellateef, A.I. Assorted kerosene-based nanofluid across a dual-zone vertical annulus with electroosmosis. *Heliyon* **2023**, *9*, e15916. [CrossRef] [PubMed]
32. Eldesoky, I.M.; Abdelsalam, S.I.; Abumandour, R.M.; Kamel, M.H.; Vafai, K. Interaction between compressibility and particulate suspension on peristaltically driven flow in planar channel. *Appl. Math. Mech.-Engl.* **2017**, *38*, 137–154. [CrossRef]
33. Jiang, F.J.; Chen, D.; Chen, J.; Li, Q.W.; Liu, Y.; Shao, X.H.; Hu, T.; Dai, J.X. Fractal analysis of shale pore structure of continental shale gas reservoir in the Ordos basin, NW China. *Energy Fuels* **2016**, *30*, 4676–4689. [CrossRef]
34. Yang, R.; Jia, A.; He, S.; Wang, T.; Hu, Q.H. Pore structure characterization and reservoir quality evaluation of analcite-rich shale oil reservoir from the Bohai bay basin. *Energy Fuels* **2021**, *35*, 9349–9368. [CrossRef]
35. Tian, H.; Pan, L.; Zhang, T.W.; Xiao, X.M.; Meng, Z.P.; Huang, B.J. Pore characterization of organic-rich lower Cambrian shales in Qiannan depression of Guizhou province, southwestern China. *Mar. Pet. Geol.* **2015**, *62*, 28–43. [CrossRef]
36. Xu, K.; Chen, S.J.; Hou, Y.T.; Lu, Z.X.; Li, C.; Han, M.M. Optimization of oil source correlation indexes: A case of Chang 10 member in Ordos Basin' Zhoujiawan area. *Arab. J. Geosci.* **2021**, *14*, 2145. [CrossRef]
37. Su, K.M.; Chen, S.J.; Hou, Y.T.; Zhang, H.F.; Zhang, X.L.; Zhang, W.X.; Liu, G.L.; Hu, G.; Han, M.M. Geochemical characteristics, origin of the chang 8 oil and natural gas in the southwestern Ordos basin, China. *J. Pet. Sci. Eng.* **2021**, *200*, 108406. [CrossRef]
38. Su, K.M.; Chen, S.J.; Hou, Y.T.; Lu, Z.X.; Shao, X.D.; Li, S.; Li, Y.; Zhu, J.; Han, M.M. Application of factor analysis to investigating molecular geochemical characteristics of organic matter and oil sources: An exploratory study of the Yanchang Formation in the Ordos Basin, China. *J. Pet. Sci. Eng.* **2021**, *208*, 109668. [CrossRef]
39. Xiao, Z.L.; Chen, S.J.; Li, Y.; Wang, P.; Ding, Z.G.; He, Q.B. The influence of bitumen on reservoir properties and hydrocarbon accumulation in the chang-8 member of Huaqing area, ordos basin, China. *Pet. Sci. Technol.* **2019**, *37*, 103–109. [CrossRef]
40. Zhang, R.; Jin, Z.J.; Liu, Q.Y.; Li, P.; Huang, Z.K.; Shi, J.Y.; Ge, Y.J.; Du, K.F. Astronomical constraints on deposition of the middle Triassic Chang 7 lacustrine shales in the Ordos basin, central China. *Palaeogeogr. Palaeoclimatol. Palaeoecol.* **2019**, *528*, 87–98. [CrossRef]
41. Teng, J.; Deng, H.C.; Xia, Y.; Chen, W.L.; Fu, M.Y. Controls of amorphous organic matter on the hydrocarbon generation potential of lacustrine shales: A case study on the Chang7 member of Yanchang formation, ordos basin, north China. *Energy Fuels* **2021**, *35*, 5879–5888. [CrossRef]
42. Yuan, W.; Liu, G.D.; Stebbins, A.; Xu, L.M.; Niu, X.B.; Luo, W.B.; Li, C.Z. Reconstruction of redox conditions during deposition of organic-rich shales of the upper Triassic Yanchang formation, ordos basin, China. *Palaeogeogr. Palaeoclimatol. Palaeoecol.* **2017**, *486*, 158–170. [CrossRef]
43. Thommes, M.; Cychosz, K.A. Physical adsorption characterization of nanoporous materials: Progress and challenges. *Adsorption* **2014**, *20*, 233–250. [CrossRef]